AIAA JOURNAL
Vol. 44, No. 12, December 2006

Crossplane Velocimetry of a Transverse Supersonic Jet in a Transonic Crossflow

Steven J. Beresh,* John F. Henfling,† Rocky J. Erven,‡ and Russell W. Spillers§
Sandia National Laboratories, Albuquerque, New Mexico 87185

DOI: 10.2514/1.22311

Stereoscopic particle image velocimetry has been employed to study the interaction created by a supersonic axisymmetric jet exhausting transversely from a flat plate into a transonic crossflow. Data have been acquired in the crossplane of the interaction at a single station in the far field, from which the velocity field identifies the induced counter-rotating vortex pair as well as the remnant of the horseshoe vortex that wraps around the jet plume as it first exhausts from the nozzle. Data taken for four different values of the jet-to-freestream dynamic pressure ratio reveal the resulting change in the vortex characteristics, where the vortex strength, size, and position are established from the derived vorticity field. Sufficient data were acquired at one condition to determine all six unique components of the turbulent stress tensor, providing the mean spatial character of the anisotropic turbulence. A measureable degree of asymmetry is observed in the size and lateral position of the counter-rotating vortex pair. Self-similarity is established laterally when dimensions are scaled by either the vortex diameter or the horizontal vortex spacing; in the wall-normal direction, scaling is found with the vortex diameter once the vortex penetration is accounted.

Introduction

THE use of supersonic jets for attitude or roll control on an atmospheric flight vehicle can actually degrade its performance because the jet exhaust plume turns over following exit from the nozzle and travels downstream where it can interfere with aft control surfaces such as fins found on bombs or missiles. Past studies have indicated that this jet/fin interaction can change the pressure field on the fins and hence the forces they generate [1–6]. This interaction is fundamentally the result of an interaction occurring upstream between the exhausting jet and the crossflowing freestream, because it establishes the flowfield structure that subsequently impinges upon the fins. The far field of the jet-in-crossflow interaction is dominated by the presence of a counter-rotating vortex pair (CVP), shown in the sketch in Fig. 1, which is induced as the jet is turned over and realigned by its encounter with the freestream. Knowledge of the vortex pair is largely extrapolated from low-speed studies in which measurements are more easily made (for example [7–11]), but these vortices have been directly detected in supersonic flowfields as well [12,13]. Additionally present are horseshoe vortices (HSV) formed when they wrap around the obstruction presented by the jet as it first exits from the nozzle, as well as the unsteady wake vortices analogous to the vortex street found in the wake of a cylinder. The strong CVP is believed to be principally responsible for the interaction with downstream fins.

The current study experimentally examines the CVP generated by a supersonic jet exhausting from a flat plate into a transonic crossflow through the use of stereoscopic particle image velocimetry (PIV) in the crossplane of the far field of the interaction, obtaining mean and turbulent velocity fields. This implementation of PIV, as compared with the streamwise PIV measurements conducted previously [14,15], directly measures the vortex structure of the jet interaction and thus is an important complement to the PIV data gathered in the streamwise plane. Although PIV has been employed by other researchers for crossplane measurements in jet-in-crossflow interactions, such data were acquired in low-speed flowfields [16,17]; supersonic applications of PIV to a jet interaction are less common and include streamwise but not crossplane measurements [18,19]. The present crossplane velocimetry expands upon a preliminary data set [20] (note that the bias error described therein has been traced to a faulty camera and is corrected in the present work) to describe the flowfield that would impinge upon a downstream fin and thus alter its performance as compared with an undisturbed flow. Additionally, these results provide jet-in-crossflow data in the sparsely studied transonic regime and offer detailed measurements of the anisotropic turbulence of the flowfield; hence, they are ideal for the validation of computational simulations and the evolution of their underlying physical models.

Presented as Paper 0906 at the 44th AIAA Aerospace Sciences Meeting and Exhibit, Reno, NV, 9–12 January 2006; received 6 January 2006; revision received 28 August 2006; accepted for publication 29 August 2006.

*Principal Member of the Technical Staff, Engineering Sciences Center; sjberes@sandia.gov. Senior Member AIAA.
†Distinguished Technologist, Engineering Sciences Center. Member AIAA.
‡Principal Technologist, Engineering Sciences Center.
§Technologist, Engineering Sciences Center.

Experimental Apparatus

Trisonic Wind Tunnel

Experiments were performed in Sandia's Trisonic Wind Tunnel (TWT), which is a blowdown-to-atmosphere facility using air as the test gas through a 305×305 mm^2 (12×12 in.^{2}) rectangular test section. The solid-wall transonic test section was used rather than the traditional porous walls, which imposes a subsonic Mach number limitation. This approach supplies a flat plate from which the jet will issue, provides computationally tractable boundary conditions for comparison of experimental data and numerical simulations, and offers improved optical access even considering the presence of the pressurized plenum enclosing the test section.

Supersonic Jet Hardware

The jet exhausted from a conical nozzle with a design Mach number of 3.73, an expansion half-angle of 15 deg, and an exit diameter of 9.53 mm (0.375 in.). The nozzle was fit to a settling chamber designed for a maximum pressure of 14 MPa (2000 psia) and instrumented to provide stagnation pressure and temperature measurements. Nitrogen was used as the working gas for the jet. The nozzle was mounted along the centerline of the top wall of the test section, which served as the flat plate from which it transversely exhausted. A side-wall window flush with the top wall was positioned downstream of the jet for viewing the far field of the interaction; a larger window in the pressurized plenum complemented the test section window. A window in the floor of

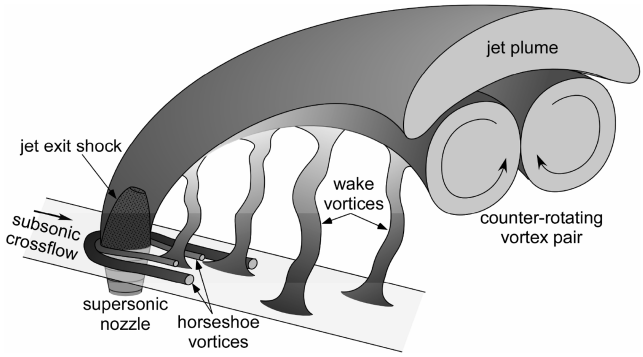

Fig. 1 Sketch of the features common to a jet-in-crossflow interaction.

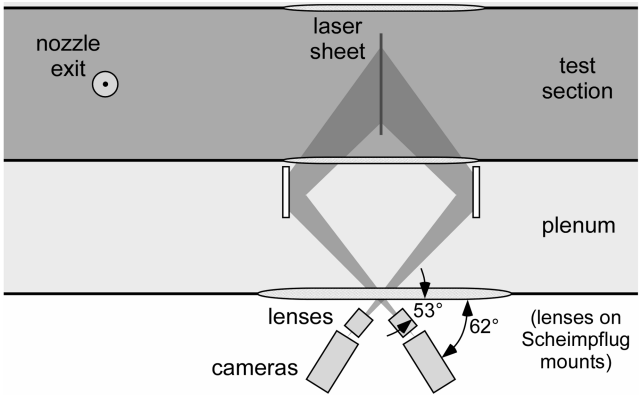

Fig. 3 Plan-view schematic of the camera arrangement for stereoscopic PIV. Flow from left to right. Not to scale.

the test section was positioned to introduce the laser sheet, which was matched by a second laser window in the bottom of the plenum. The relative location of the jet and windows within the test section is sketched in Fig. 2, which additionally shows the laser sheet for the crossplane PIV measurements and side-wall pressure taps for measuring the test section static pressure used to determine the freestream Mach number.

Particle Image Velocimetry System

The present PIV measurements were acquired with the laser sheet normal to the wind-tunnel axis, as shown in Fig. 2, and aligned to the midpoint of the side-wall window. This placed the measurement location 321.8 mm downstream of the jet nozzle centerline, corresponding to 33.8 jet diameters. The coordinate system is chosen such that the u component lies in the streamwise direction and the v component is in the vertical direction, positive away from the top wall; the w component is chosen for a right-handed coordinate system. The origin is located at the center point of the jet nozzle exit plane.

The light source was a pair of frequency-doubled Nd:YAG lasers (Coherent Infinity 40–100) that were operated at 5 Hz producing about 120 mJ per beam. The beams were combined and formed into coplanar sheets and directed into the test section. The crossplane PIV configuration aligns the freestream direction of the wind tunnel with the out-of-plane motion through the laser sheet; therefore, to limit the resulting particle dropout, the experiment used a thick laser sheet of 2.0 mm and a short time between pulses of 1.80 μs. These conditions were found to be sufficient to consistently obtain correlations from the image pairs without inducing bias errors from particle dropout.

The TWT is seeded by a thermal smoke generator (Corona Vi-Count 5000) that produces a large quantity of particles typically 0.2–0.3 μm in diameter from a mineral oil base. The smoke generator is contained within a pressurized tank to force the smoke through a duct into the elevated pressure of the TWT's stagnation chamber, where injector tubes distribute the particles and the subsequent flow conditioning section removes any disturbances induced by particle injection and assists in dispersing the particles. The jet itself remains unseeded. Although this creates a serious measurement bias near the jet exit due to selective flow sampling, data acquired further downstream are not subject to such a difficulty because turbulent mixing entrains particles from the freestream and spreads them throughout the interaction once in the far field. The particles are sufficiently small that they rapidly attain the local velocity once they have been redistributed [21,22] and the particle density is great enough even within the vortices that strong correlations are routinely found.

Scattered laser light was collected by frame-straddling CCD cameras (Redlake MegaPlus ES4.0/E), with a resolution of 2048 × 2048 pixels and digitized at 8 bits. Each camera was connected to its own computer with digital input/output boards and operated at 5 image pairs per second, synchronized for the two cameras. Commercially available software was used to control the cameras and computer hardware (SpeedVision OmniSpeed) and timing synchronization between the cameras and lasers was accomplished using two digital delay generators (Stanford Research Systems DG535). The cameras were equipped with 105 mm lenses (Nikon Micro-Nikkor) operating at $f/4$ and placed upon Scheimpflug lens mounts to achieve an oblique focal plane.

The camera arrangement is shown in Fig. 3. Both cameras looked through the same window of the test section, viewing the laser sheet from opposite directions, because placing one camera at the other side-wall window precludes access to the test section. To improve upon the limited camera viewing angles due to the constricted optical access, mirrors were rigidly mounted inside the plenum to reflect

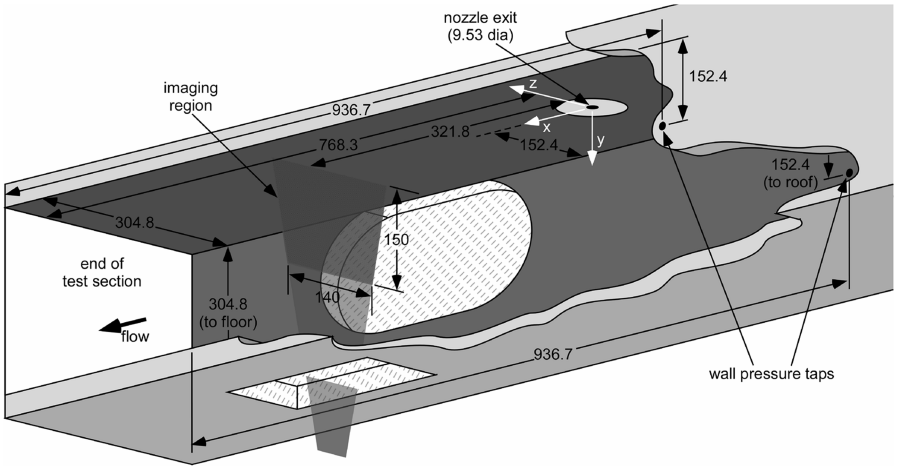

Fig. 2 Schematic of the experimental configuration, looking downstream from beneath the wind tunnel. Flow from right to left. All dimensions in millimeters. Not to scale.

scattered laser light to the cameras at a sharper angle, as illustrated in Fig. 3; wind-tunnel vibrations have been found not to pose a difficulty at subsonic conditions. This allowed an angle of 53 deg between the camera lenses and the normal to the laser sheet, which is greater than desired but the best achievable given the optical access. The limited optical access prevents meaningful movement of the imaging location upstream or downstream in the wind tunnel, thus all data in the present document have been acquired at a single position located at the center of the side-wall window.

To calibrate the stereoscopic system, the distorted sheet procedure described by Soloff et al. [23] has been used, alternatively known as a "thick sheet" or multiplane calibration. An aluminum plate 3.05 mm (0.120 in.) thick and flat to within 0.05 mm (0.002 in.) was fabricated with holes drilled every 12.7 mm (0.500 in.) as fiduciary marks. Both surfaces of the plate had been sandblasted to create speckle patterns when illuminated, upon which the PIV software can correlate as the target is translated through the measurement region. Green LED lamps were used for illumination during the calibration process as they were found to create sharper speckle patterns than white light, as well as providing a narrow wavelength that nearly matched that of the laser. This ensured no refocusing due to chromatic aberration. The calibration target was precisely aligned normal to the test section axis and was situated on a translation stage positioned to move the target along this axis. A sequence of images was acquired by each camera as the target was traversed a distance sufficient to ensure that both target surfaces translated fully through the laser sheet thickness. The resulting calibration images were used by the data-processing software (IDT's ProVision 2.02) to tie together the two sets of image pairs to produce three-dimensional vectors.

Sequences of 100 or 150 image pairs from each camera were acquired during each wind-tunnel run. Captured images retain a trapezoidal appearance due to the divergence of the laser sheet. Images were interrogated with a 64×64 pixel window employing adaptive correlations and a spatial offset to account for the mean streamwise particle displacement. The spatial resolution varies across the image due to the varying magnification of the oblique camera view, yielding 9.3 mm horizontally and 5.9 mm vertically, when measured at the wind-tunnel centerline. An approximate 50% overlap in adjacent interrogation windows typically was used to oversample the velocity fields. The resulting vector fields were validated based upon signal-to-noise ratio and nearest-neighbor comparisons.

Experimental Conditions

The freestream Mach number is $M_\infty = 0.8$ with a wind-tunnel stagnation pressure $P_0 = 154$ kPa (22.4 psia). The wind-tunnel Reynolds number at these conditions is 20×10^6 m^{-1} (6×10^6 ft^{-1}). The nominal stagnation pressure for the Mach 3.73 jet is $P_{0j} =$ 4.96 MPa (720 psia), providing a centerline jet exit pressure of $p_e = 47.1$ kPa (6.84 psia). These conditions combine to produce a nominal jet-to-freestream dynamic pressure ratio $J = 10.2$. Additional cases span a range of J values while maintaining $M_\infty = 0.8$; compensation for the changing wind-tunnel blockage was provided by shifting the choke mechanism. All cases were chosen such that the freestream static pressure $p_w = 101$ kPa (14.7 psia); therefore, the jet was always overexpanded. This wall pressure was measured from the mean of two static pressure taps located on the wind-tunnel side walls 168 mm upstream of the jet nozzle centerline, as seen in Fig. 2. Table 1 summarizes the key parameters for the four test cases, including M_∞ and the velocity reference U_∞ as calculated isentropically from the ratio p_w/P_0 and the stagnation temperature T_0, as well as $U_\infty(x)$ determined from the actual PIV data (discussed below).

Table 1 Experimental conditions for the jet and wind tunnel

Case	J	M_∞	P_0, kPa	P_{0j}, MPa	U_∞, m/s	$U_\infty(x)$, m/s
1	16.7	0.80	154	8.14	286	290
2	10.2	0.80	154	4.97	286	281
3	5.6	0.80	154	2.76	286	280
4	2.8	0.80	154	1.36	286	278

The gas supply for the jet was unheated, so the jet stagnation temperature T_{0j} varied from 296 K to 307 K (533–553 R) depending upon the laboratory ambient conditions. The wind-tunnel air supply is heated in the storage tanks, but not temperature controlled subsequent to this; therefore the freestream stagnation temperature T_0 also is subject to slight variation and fluctuates from 324 to 329 K (582–591 R).

The 99%-velocity boundary layer thickness has been measured as 14.8 ± 0.4 mm (0.58 ± 0.02 in.) from PIV data acquired in the streamwise plane [14]. This measurement was acquired on the wind-tunnel centerline 254 mm downstream of the usual center point of the jet nozzle exit, though the nozzle had been replaced by a blank for these measurements.

For the primary case of $J = 10.2$, 29 wind-tunnel runs totaling 4000 instantaneous realizations of the PIV velocity field were collected, which is sufficient for convergence of turbulent quantities. The other three cases each were conducted over five wind-tunnel runs totaling 550 realizations, which were intended for mean data only.

Results

Velocity and Turbulent Stress Fields

Mean velocity data are shown in Fig. 4 for all four values of J, calculated from all available instantaneous realizations. In-plane velocities are displayed as vectors superposed upon a contour plot of the out-of-plane (streamwise) velocities. The axes have been normalized to the jet exit diameter d_j and velocities are normalized to the freestream velocity U_∞. In-plane velocity bias errors stemming from the stereoscopic camera calibration have been corrected using undisturbed freestream data as described in [20], in which the lateral motion is known to be nearly zero as determined by wind-tunnel flow angularity studies, and hence can be assumed to result principally from measurement bias. Out-of-plane velocity biases remain uncorrected primarily because this component of the error unidentifiably varies with J and hence cannot be corrected using jet-off measurements.

The vector fields in Fig. 4 clearly show the CVP induced by the jet-in-crossflow interaction, which is centered near the lower portion of the streamwise velocity deficit revealed by the contours. This is consistent with two-dimensional PIV data acquired along the wind-tunnel centerline, which showed the vortex pair to be situated below the decaying jet [14]. The streamwise velocity deficit displays the kidney bean shape characteristic of jet-in-crossflow interactions; ample precedent exists for a velocity deficit rather than an excess for compressible flows [12,13,24–26], where [25] most nearly replicates the conditions of the current experiment. It also is evident that a narrow wake exists along the centerline, where the streamwise velocity has not fully recovered; this, too, was observed in the two-dimensional PIV [14]. Finally, strong streamwise velocity deficits near the wall within the boundary layer indicate the remnant of the HSV that forms around the jet plume immediately after exit from the nozzle. Vortical motion is visible in the HSV velocity vectors for the two larger J values, but clearly possesses an appreciably smaller magnitude than that associated with the CVP.

The four cases of Fig. 4 show how the flowfield changes with the strength of the jet. It is evident that the size of the jet and the CVP as well as their distance from the wall increase as J becomes larger, consistent with the earlier streamwise measurements [14]. Larger J induces stronger in-plane velocities associated with the CVP. Furthermore, the streamwise velocity deficit induced by the jet can be seen to increase slightly for greater J while its size expands markedly. A similar trend is evident in the horseshoe vortices. Interestingly, it appears that the HSV combines into one structure for $J = 2.8$, which is consistent with the trend of narrowing distance between these two vortices as J is lowered. However, this instead may be a result of limits in the spatial resolution of the measurements. More subtly, the freestream velocity is found to be somewhat greater at higher J than lower, despite constant M_∞. This is due to the added

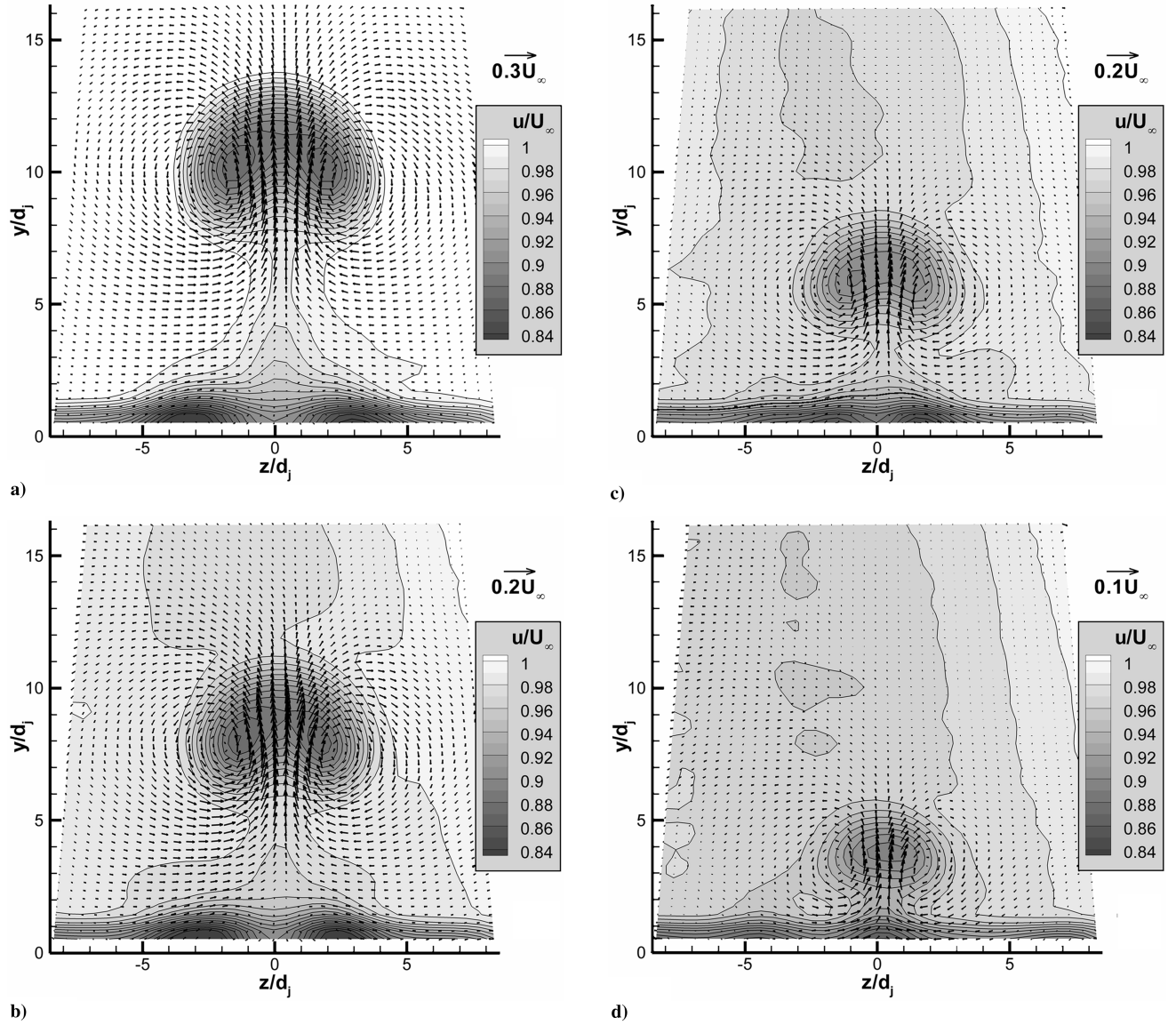

Fig. 4 Mean velocity fields for varying J at $M_\infty = 0.8$ in the crossplane 33.8d_j downstream of the jet nozzle centerline. In-plane velocities are displayed as vectors superposed upon a contour plot of the out-of-plane (streamwise) velocities. a) $J = 16.7$; b) $J = 10.2$; c) $J = 5.6$; d) $J = 2.8$.

blockage in the solid-wall test section for the larger jet found at higher J, which causes a greater rise in M_∞ from the constant value established at the upstream pressure taps. A more extensive discussion of this phenomenon is found in [14]. The lateral variation in the streamwise velocity away from the influence of the interaction has been shown to result from measurement error.

Vorticity fields of the crossplane motion are easily calculated from the in-plane velocities using a finite-difference scheme and are shown in Fig. 5, normalized by d_j and U_∞. Note that the positive vorticity axis is into the page, as this is the direction of the positive x axis. For all four values of J, the vorticity due to the CVP is clearly depicted, but the HSV in the boundary layer is only weakly detected. This is expected from the velocity fields of Fig. 4, as the in-plane vectors do not show the presence of the HSV as strongly as does the out-of-plane velocity. The vortex centers as determined by the vorticity fields are found somewhat closer to the interaction centerline than the centers of rotation visualized by the velocity fields; this occurs because the influence of the opposite vortex in the CVP is superposed upon the velocities but minimally impacts the vorticity.

All six unique components of the turbulent stress tensor may be found for the $J = 10.2$ case, in which a sufficient quantity of data was gathered to achieve statistical convergence. These results are shown in Fig. 6. Qualitatively, each plot displays a somewhat different shape, indicating that the stress components do not adhere to a common distribution. The streamwise stress $\overline{u'^2}$ approximately tracks the streamwise velocity deficit of Fig. 4b both in shape and intensity variation, but the vertical stress $\overline{v'^2}$ is concentrated toward the centerline whereas the lateral stress $\overline{w'^2}$ is greatest near the vortex centers. This generally is consistent with the location of greatest intensity in each of the respective mean velocity components. Similarly, the three turbulent shear stresses each exhibit distinctly different distributions. The distributions for the shear stresses are noticeably thinner than those for the normal stresses, where $-\overline{u'v'}$ follows the upper and lateral edges of the interaction at which mixing occurs with the crossflow, whereas $-\overline{u'w'}$ and $-\overline{v'w'}$ display activity nearer the vortex cores. It also is evident that the magnitude of $\overline{v'^2}$ exceeds the magnitude of the other two normal stresses, whereas the two shear stress components containing a v' term have greater magnitude than the one that does not. From the former observation, it is apparent that the turbulence is distinctly anisotropic, consistent with similar observations in the streamwise plane [15].

The turbulence kinetic energy k, which is of considerable interest given its prominence in turbulence models, is easily derived from the turbulent normal stresses in Figs. 6a–6c and is provided in Fig. 7. The distribution of k possesses the familiar kidney bean shape previously seen for the streamwise velocity deficit and the $\overline{u'^2}$ and $\overline{v'^2}$ fields. The

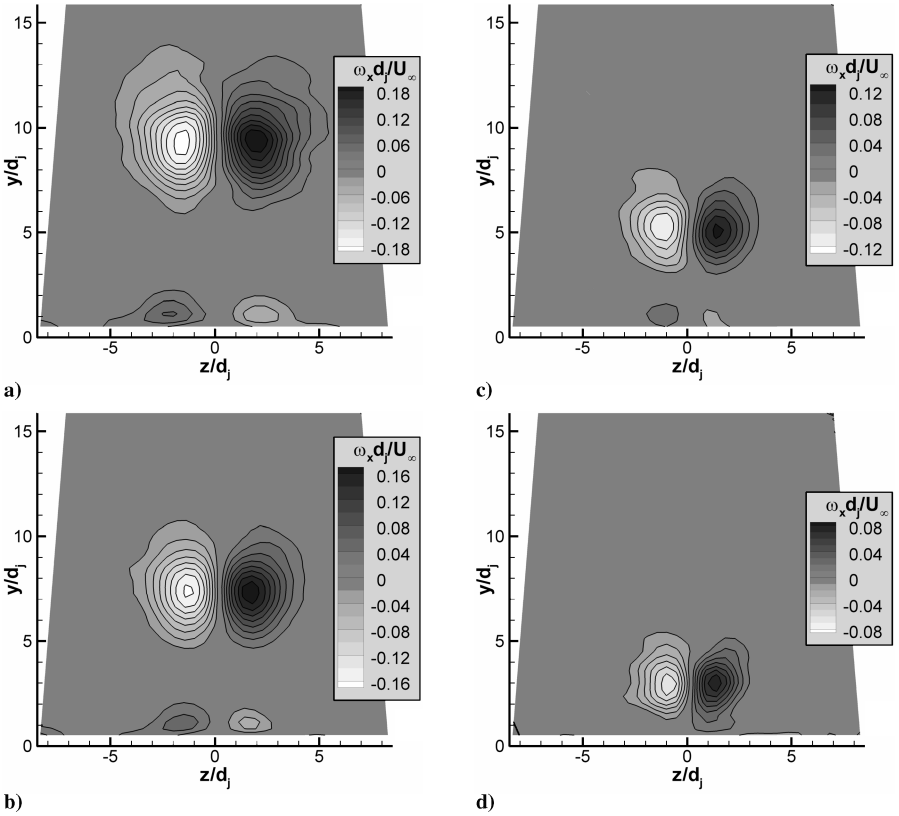

Fig. 5 Mean vorticity fields derived from the velocity data of Fig. 4. a) $J = 16.7$; b) $J = 10.2$; c) $J = 5.6$; d) $J = 2.8$.

narrow jet wake and the HSV are visible as well, though the energy contained within them is relatively small.

Uncertainty Analysis

The uncertainty of the velocity measurements is separable into two components: a precision error due to PIV correlation noise, experimental repeatability, and data convergence error; and a bias error arising principally from the PIV calibration. The precision error is assessed straightforwardly using multiple wind-tunnel runs for the $J = 10.2$ case, from which the precision uncertainty was found as the 95% confidence interval of the scatter in the measurements. These results include the effect of variations in J and M_∞ among runs comprising a mean test condition, typically ± 0.1 and ± 0.002, respectively.

The bias component of the error could not realistically be transformed into a precision error through the use of multiple calibrations, as was accomplished for the earlier two-dimensional streamwise measurements [14,15]. Partly, this is because the calibration process is too difficult and time-consuming to perform repeatedly, and partly it is because the calibration bias is substantially reproducible. Instead, the calibration bias was found by reinstating the calibration target into the measurement location and traversing it a known distance in two dimensions corresponding to the expected particle motion in the time between laser pulses, then processing the resulting images as if they were PIV data. Bias values were found from the deviation of the measured translation with the actual motion. Because the target was aligned to the wind tunnel in the same fashion as for acquiring calibration images, this procedure accounts for biases produced by the calibration algorithm and not those arising from a misalignment with the actual laser sheet position; the implications of this deficiency are addressed in [27]. Though the in-plane components of the calibration bias have been corrected using freestream measurements, it is unclear to what extent this reduces the uncertainty; therefore it is conservative to estimate the total uncertainty including the calibration bias. Combining all enumerated error sources, uncertainties in the 3-D crossplane measurements were calculated as ± 9 m/s, ± 4 m/s, and ± 6 m/s in the u, v, and w components, respectively, which equate to $0.03U_\infty$, $0.015U_\infty$, and $0.02U_\infty$, respectively.

Regarding the turbulent stresses, the precision component of the uncertainty was determined in the same manner as the mean velocity uncertainties, by examining the deviation between multiple wind-tunnel runs. The effect of the calibration bias upon turbulent quantities is somewhat more complicated, as additive bias errors will subtract out when the turbulent fluctuations are calculated, but multiplicative biases will not. To be conservative, the entire bias error is assumed to be multiplicative and the same scaling error seen over the mean velocity range to apply linearly to the velocity fluctuations. Still, the calibration bias error affects the turbulent stresses less than the mean velocities because the fluctuation magnitudes are smaller than those of the mean velocities, particularly in the streamwise direction.

Additional wind-tunnel runs were conducted for the $J = 10.2$ case in which the time between laser pulses was varied from the standard value. Changing this parameter by a reasonable amount did not significantly alter the results, indicating that out-of-plane motion did not induce a bias error by selectively removing some particles from the PIV correlations.

Velocity and Turbulent Stress Profiles

A more direct comparison of the data for the different values of J can be made by considering velocity profiles extracted from the PIV field data and displayed on the same plot. Figure 8 shows the streamwise and vertical velocity components along the wind-tunnel centerline ($z = 0$); the lateral component w is not shown because it is effectively zero along this line, as can be deduced from the vector plots of Fig. 4 (and in fact is measured as zero, to within the uncertainty). The streamwise component is given as a velocity deficit from the local freestream velocity $U_\infty(x)$; these values (given in Table 1) are found from the topmost vectors in the velocity field, outside the influence of the interaction, to distinguish them from the U_∞ found from the upstream pressure taps, which do not capture the dependence on downstream distance due to increasing flowfield blockage. A striking attribute of Fig. 8a is that the uncertainty is

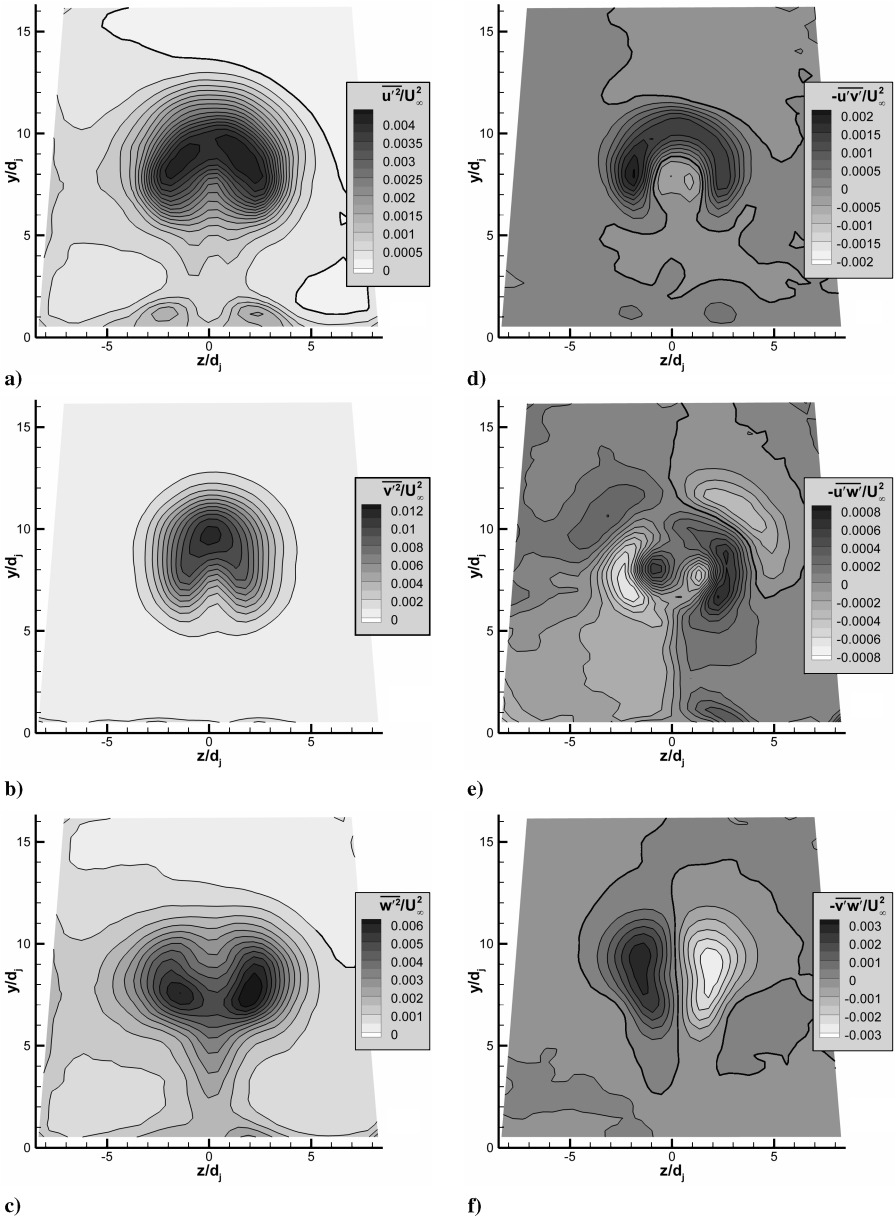

Fig. 6 Turbulent stresses for $J = 10.2$ and $M_\infty = 0.8$ in the crossplane 33.8d_j downstream of the jet nozzle centerline.

particularly large relative to the magnitude of the streamwise velocity deficit. This is partly because the velocity deficit is only a small portion of U_∞, and partly because the uncertainty is greatest in the out-of-plane component of velocity. In contrast, the uncertainty for v in Fig. 8b is a considerably smaller fraction of the vertical velocity magnitude.

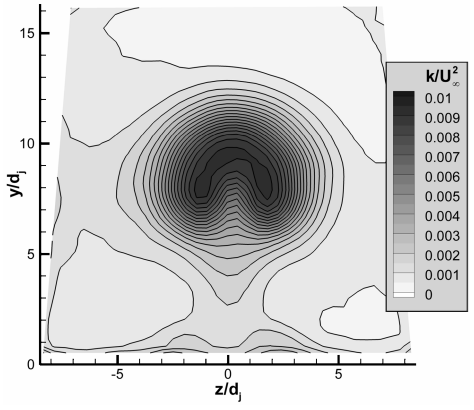

Fig. 7 Turbulent kinetic energy for $J = 10.2$ and $M_\infty = 0.8$.

From Fig. 8a, it is evident that the small increase in streamwise velocity deficit with J is scarcely significant in relation to the measurement uncertainty. However, [14] indicates that this trend is real, though more pronounced farther upstream than at the present location. The width of the profile also can be seen to increase with J, reflecting the larger size of the jet that induces the deficit. The deficit near the wall is due to the boundary layer, and at $J = 16.7$, the jet wake is visible where the profile fails to return to zero between the jet and boundary layer. The increase in the magnitude of v as J grows larger, shown in Fig. 8b, is much more distinct than that in the u deficit, as is the increase in the width of the curve. This behavior is a function of the expanding size and strength of the CVP. The presence of the HSV can be noted in the slightly negative region of v near the wall, excepting the $J = 2.8$ case. Although the rotation of the HSV is small and difficult to discern in the vector fields of Fig. 4, the extracted velocity profiles identify it more clearly.

The turbulent stresses also have been extracted along the wind-tunnel centerline and are shown in Fig. 9 for $J = 10.2$, the only condition at which these data are available. Figure 9a indicates that the peaks of the streamwise and vertical components of the normal

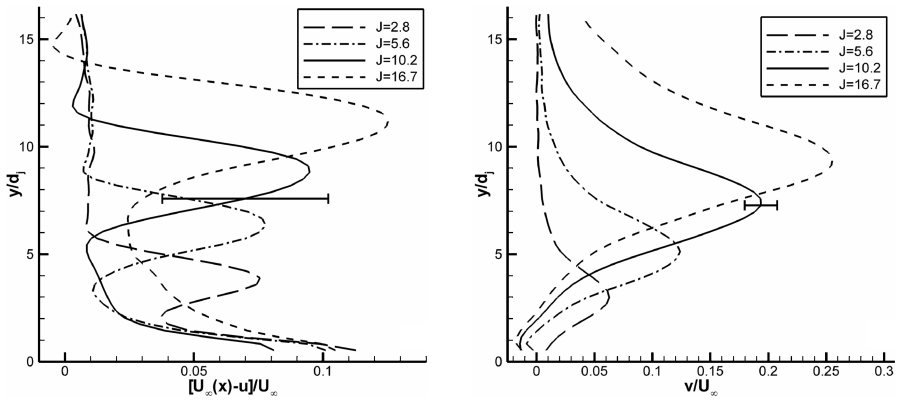

Fig. 8 Mean velocity profiles along a line extracted at the wind-tunnel centerline ($z = 0$). a) streamwise velocity deficit; b) vertical component.

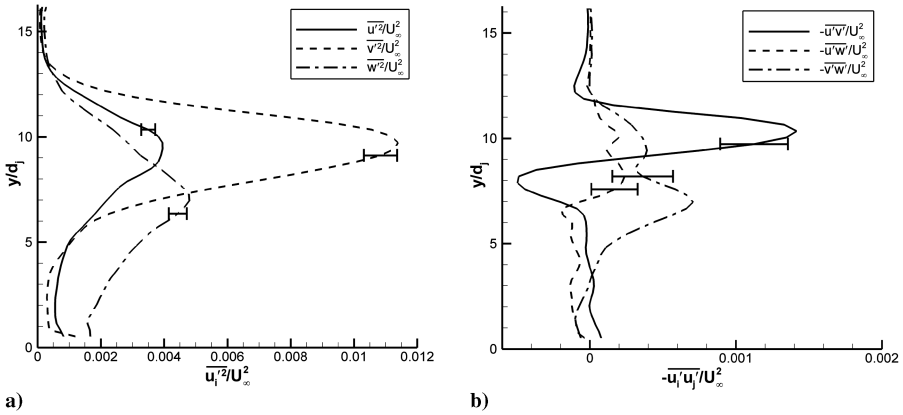

Fig. 9 Turbulent stress profiles for $J = 10.2$ along a line extracted at the wind-tunnel centerline ($z = 0$). a) normal stresses; b) shear stresses.

stresses occur at the same vertical position, which approximately coincides with the peak of the streamwise velocity deficit (more definitively established in [15]), but the peak of the lateral component lies closer to the wall. The inflection point of the $-\overline{u'v'}$ curve in Fig. 9b also coincides with the streamwise velocity deficit peak, but the other two shear stresses are too noisy to meaningfully comment upon them; Figs. 6e and 6f show this is because the effects of $-\overline{u'w'}$ and $-\overline{v'w'}$ principally lie off the centerline.

It is of additional interest to examine the velocity profiles along lines through the vortex centers of the CVP, though the selection of these profile locations is complicated by a small but observable asymmetry in the interaction. Figure 4 shows that the centers of rotation of the left and right vortices (of negative and positive vorticity, respectively) in the CVP are not symmetrically located across the wind-tunnel centerline. For example, at $J = 10.2$ the negative vortex appears centered at about $z/d_j = -2.0$, whereas the positive vortex is centered at about $z/d_j = 2.5$. This asymmetry is borne out by the vorticity fields in Fig. 5, which show the negative and positive vortices centered at $z/d_j = -1.5$ and $z/d_j = 2.0$, respectively. Such behavior is not unprecedented, as other jet-in-crossflow studies have detected asymmetric vortices produced by nominally symmetric flowfield geometries [12,28,29]. To account for this effect, off-centerline velocity profiles have been extracted through the centroid of each vortex in the CVP at each value of J; therefore each of these profiles is located at a different z/d_j. (The procedure for locating the vortex centroid is described in the section below). Figure 10 shows the results for the mean velocities, where the profiles through the negative vortices are given by the dark lines and those through the positive vortices are given by the gray lines. The profiles of w for the positive vortices have been inverted in sign to compensate for the opposite direction of rotation.

Figure 10a shows profiles of the streamwise velocity deficit that are very similar to those through the wind-tunnel centerline in Fig. 8a, save that their peaks occur somewhat closer to the wall, as predicted by the kidney bean shape in Fig. 4. Based on Fig. 4, profiles of v would be expected to be near zero because a vertical line through the center of rotation of each CVP vortex will show motion only in the w component. However, the centroid of each vortex is actually found nearer to the wind-tunnel centerline than the center of rotation suggested by the vector fields, which leads to the nonzero values of v shown in Fig. 10b. This effect substantially exceeds the measurement uncertainty. The v profiles are more asymmetric in y than their counterparts at $z = 0$ and possess a smaller magnitude, with their peaks occurring nearer the wall than the maximum streamwise velocity deficit. Again, a small degree of negative velocities is seen near the wall due to the HSV. The inflection points of the w profiles appear to lie a little farther from the wall than the maximum v component, though this effect lies within the experimental uncertainty. It is noteworthy that the magnitude of w is greater for the lower half of the vortex than the upper. Coupled with the observed asymmetry in the v profiles, this indicates that the vortices do not possess a horizontal axis of symmetry despite the appearance of the vorticity contours in Fig. 5, which presumably results from the influence of the wall.

Figure 11 shows the turbulent stress profiles for $J = 10.2$ along the same vertical lines through the vortex centroids. As was the case at $z = 0$, the peak locations for $\overline{u'^2}$ and $\overline{v'^2}$ are found at approximately the same distance from the wall as the peak in u, but the peak for $\overline{w'^2}$ lies nearer the wall. The magnitude of $\overline{u'^2}$ is about the same as at $z = 0$, whereas the magnitude of $\overline{v'^2}$ has diminished and that of $\overline{w'^2}$ has increased; these observations are simply a different presentation of those from Fig. 6 and reflect the prominence of the lateral velocity

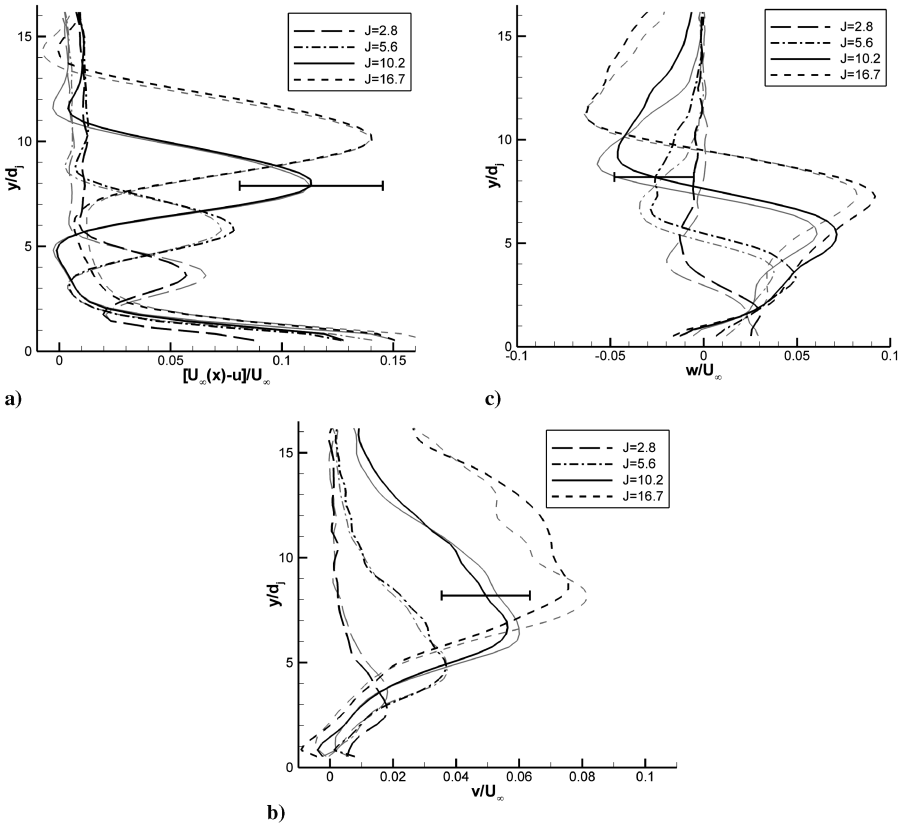

Fig. 10 Mean velocity profiles through the centroid of each vortex in the CVP. Dark lines show the negative vortex and gray lines the positive vortex. a) Streamwise velocity deficit; b) vertical component; c) lateral component. Profiles of *w* have been inverted in sign for the positive vortex.

component of the vortical motion along a vertical profile near its center of rotation. Similarly, the turbulent shear stresses of Fig. 11b show that $-\overline{u'v'}$ maintains about the same magnitude, though it no longer has a significant negative region, whereas $-\overline{v'w'}$ has grown dominant off the wind-tunnel centerline.

Figures 10 and 11 demonstrate that the velocity profiles through the centers of the positive and negative vortices are identical to within the measurement uncertainty, though they are located at somewhat different lateral distances from the wind-tunnel centerline. This suggests that the interaction is symmetrical, but displaced to one side of the wind tunnel. The issue of symmetry is explored further below.

The data extracted along the wind-tunnel centerline can be compared to the corresponding two-dimensional PIV acquired in the streamwise plane, principally as a means of assessing the measurement accuracy. This introduces a topic beyond the scope of the present document; therefore it is treated in detail in [27]. In brief, agreement is generally good though sometimes slightly in excess of the uncertainty estimates, but certainly sufficient to establish the veracity of the measured flow structure.

Vortex Characteristics

The CVP can be defined by the strength, size, and position of each of the two vortices. The previous streamwise PIV measurements [14] provided some inference of this knowledge, but the present work allows for an explicit characterization of the vortices at the measured crossplane position. The principal approach to determining the vortex positions and strengths employed an integration of the vorticity magnitude for each vortex in the CVP. The integrated vorticity Γ_x (i.e., the circulation) was computed as per

$$\Gamma_x = \int \omega_x \, \mathrm{d}A \tag{1}$$

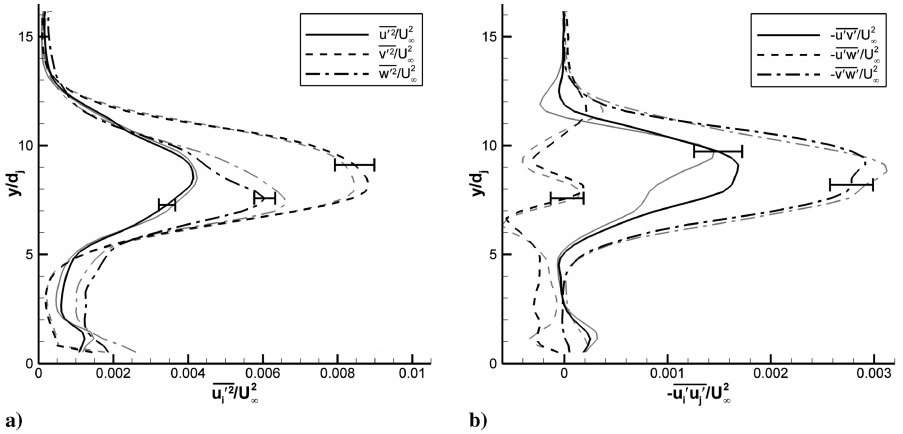

Fig. 11 Turbulent stress profiles for $J = 10.2$ through the centroid of each vortex in the CVP. Dark lines show the negative vortex and gray lines the positive vortex. a) normal stresses; b) shear stresses.

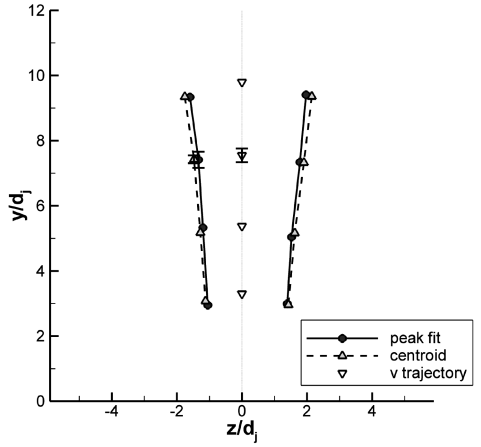

Fig. 12 Position of each vortex in the CVP as found by peak fits and centroids; negative vortex on the left and positive vortex on the right. Also given are trajectory positions from vertical velocity profiles in [14].

by numerically integrating the measured vorticity field over an area whose perimeter was defined by first locating the locus of points 37% $(1/e)$ of the maximum vorticity for that particular case, then extending the perimeter until the slope at each point intersected zero vorticity to better capture the entirety of the vortex. This threshold is somewhat arbitrary in that it was selected not for any physical reason, but because it was found to consistently produce a sensible definition of the vortices; lower thresholds tended to incorporate noise from the vorticity field, especially at lower values of J. The centroid of the vortex was found over the same perimeter by

$$(\bar{y}, \bar{z}) = \frac{1}{\Gamma_x} \int (y, z)\omega_x \, \mathrm{d}A \tag{2}$$

Figure 12 presents the position of each vortex in the CVP both by the centroid method described above and by the peak position of a paraboloid fit to the vorticity field in the vicinity of its maximum. As can be seen, both methods provide nearly identical answers, which helps validate the integration boundary described above. Also shown are the positions found at the present crossplane location from the centerline trajectories established in [14] using the maxima in the vertical velocity component. Uncertainty estimates were found using repeated measurements for the $J = 10.2$ and $M_\infty = 0.8$ case to quantify the precision error. Bias errors are generally of low spatial frequency across the field and hence do not appreciably contribute to the derivatives used to compute the vorticity; the principal bias source for Fig. 12 is simply the precision of positioning the calibration target in the wind tunnel. Error bars are shown for the vertical position, but the same uncertainty magnitude applies in the horizontal direction as well. The vortex vertical positions are seen to coincide with the trajectory position derived from the centerline vertical velocity, to within the measurement uncertainty, which indicates that this velocity component does provide a means of tracking the CVP as suggested in [14]. Figure 12 clarifies earlier observations concerning the interaction asymmetry by quantitatively showing that the positive vortex always lies farther from the wind-tunnel centerline than the negative vortex, creating the horizontal displacement of the interaction; the vertical positions of the two vortices are identical to within the uncertainty. It is not known if the interaction asymmetry witnessed at this downstream location represents the amplification of an imperceptible perturbation or misalignment at the nozzle exit, or if instead responsibility lies with a small asymmetry in the wind-tunnel freestream itself.

The vortex size also is determined using two different methods. One approach is to integrate the area within the contour used to determine the circulation Γ_x and then characterize the vortex by its diameter d_Γ as if it were circular. A second approach instead determines d_Γ from the locus of points at which the velocity tangential to the vortex center v_t is a maximum along a radial arm. Figure 13 shows these data for both vortices, from which it can be

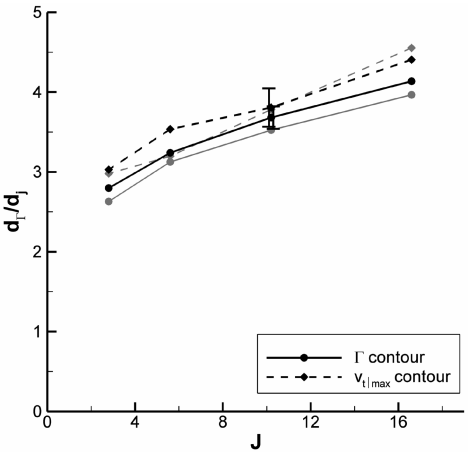

Fig. 13 Size of each vortex in the CVP as found by the vortex circulation contour and by the locus of maximum tangential velocity. Dark lines show the negative vortex and gray lines the positive vortex.

seen that the results are essentially the same, particularly given the larger uncertainty when employing the $v_{t,\max}$ method. As expected, greater values of J produce larger vortices. It also is shown that the negative vortex generally is larger than the positive vortex; though this observation is within the uncertainty for the $v_{t,\max}$ contour, it is consistent and slightly in excess of the uncertainty for the Γ_x contour. Therefore, the perceived difference in vortex size suggests that the asymmetry in the flowfield is more substantial than a simple displacement of the vortices off the centerline of the wind tunnel. Other experiments that have detected interaction asymmetry also have noted that the two vortices differ in size as well as position [12,28,29].

The vortex strengths of the CVP are given in Fig. 14, both by the maximum of the paraboloid peak fit and by the vortex circulation. Negative values of vorticity and circulation have been inverted to allow a comparison between the two vortices. Although each approach shows increasing magnitudes with larger J, the circulation increases with a more linear character as compared with the peak vorticity. The uncertainties are too large to determine whether the positive or negative vortex consistently possesses a greater magnitude than the other, and hence any contribution to the interaction asymmetry is indeterminate.

Similarity analyses performed for incompressible jet-in-crossflow interactions suggest that proper scaling of the interaction parameters can produce commonality despite varied values of J. For example, Keffer and Baines [30] demonstrate that scaling lateral velocity profiles by a measure of the interaction width produces self-similarity in the far field for a range of J; Smith and Mungal [28] find analogous

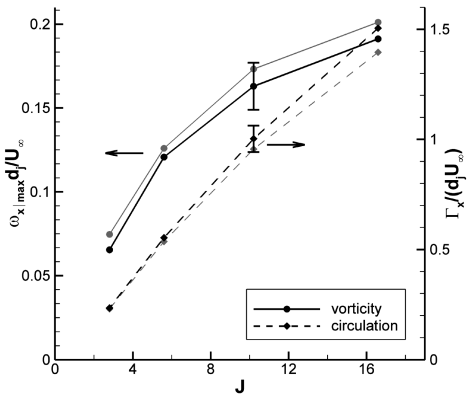

Fig. 14 Strength of each vortex in the CVP as found by the maximum vorticity magnitude (left axis) and the vortex circulation (right axis). Dark lines show the negative vortex and gray lines the positive vortex.

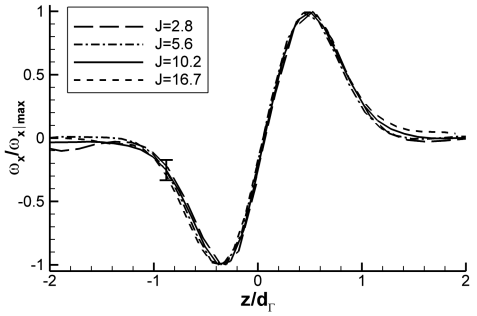

Fig. 15 Vorticity along a horizontal line through the centroid of the CVP, where vorticity is normalized by its maximum and distance by the vortex diameter.

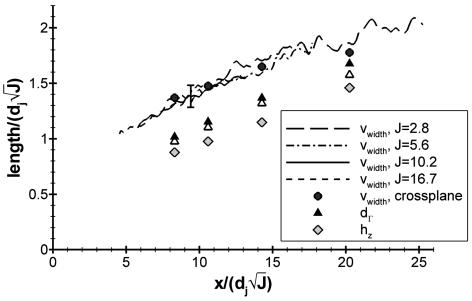

Fig. 17 Vortex length scales normalized by $\sqrt{J}$. Shown are the width of the vertical velocity profile from [14] (four lines), the analogous data from the present crossplane measurements (circles), the vortex diameter for the negative vortex (solid triangles) and the positive vortex (empty triangles), and the horizontal vortex spacing (diamonds).

results from concentration profiles. With this as inspiration, Fig. 15 plots traces of the vorticity along a horizontal line through the centroid of the CVP, where the z axis has been normalized by the vortex diameter d_Γ taken from Fig. 13 and the vorticity is normalized by $\omega_{x,max}$ from Fig. 14. As these normalization values differ for the negative and positive vortices, due either to asymmetry or measurement uncertainty, each lateral half of the plot is normalized by mildly different values to compensate. Figure 15 demonstrates that the collapse of the data is quite good. Comparable results may be found by instead normalizing the z axis by the horizontal vortex spacing h_z as taken from the centroid calculations of Fig. 12. Similarity using the vortex separation is consistent with its use as a governing parameter in various semiempirical models [8,31,32], but Fig. 15 demonstrates that the vortex diameter works equally well.

Comparable success when analyzing vertical vorticity profiles through the vortex centroids, analogous to the velocity profiles of Fig. 10, is achieved only when employing both d_Γ and the vertical position of the CVP centroid h_y. Figure 16 shows the results when the y axis is aligned by h_y then normalized by d_Γ, and the vorticity is normalized by $\omega_{x,max}$; again, different values are used for the negative and positive vortices. As in Fig. 15, the profiles are found to collapse to within the measurement uncertainty. Taken together, these results suggest that the vortex diameter serves as an appropriate scaling parameter for the growth of the CVP size once the penetration of the vortices into the crossflow is taken into account.

It would be preferable to determine similarity based upon the flow conditions that establish the interaction rather than a characteristic of the induced CVP. Previous studies have indicated that the trajectories for the jet and the CVP each collapse to a single curve when dimensions additionally are normalized by J [30,33], which was confirmed to hold reasonably well for the present study by the streamwise PIV measurements [14]. However, the full-width half-maximum of the vertical velocity profiles v_{width}, which was used as an inference of the length scale for the CVP, did not exhibit collapse when normalized by J [14]. Pratte and Baines's work suggests that lateral length scales exhibit similarity when instead normalized by $\sqrt{J}$ [34]; when the v_{width} profiles from [14] are plotted in such a fashion in Fig. 17, they exhibit excellent collapse. Unfortunately, it is not straightforward to examine the collapse of the crossplane CVP length scales because all the data were acquired at the same downstream location, which become different positions when normalized by $\sqrt{J}$. Figure 17 shows values of v_{width} determined from the centerline of the current crossplane measurements corresponding to the four values of J, which agree with the streamwise trajectories to within the measurement uncertainty. Data points for the vortex diameter d_Γ, both for the negative and positive vortex of the CVP, and for the horizontal vortex spacing h_z are given as well, which naturally yield different magnitudes from v_{width} but display apparently similar slopes. Lacking additional crossplane measurement stations, no better examination of similarity in the downstream evolution of vortex scales is possible.

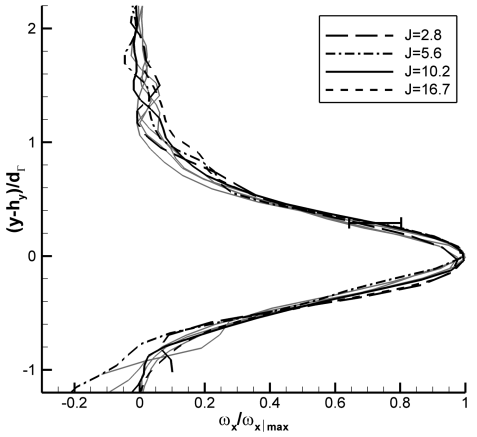

Fig. 16 Vorticity along a vertical line through the centroid of each vortex in the CVP, where vorticity is normalized by its maximum and distance by the vortex diameter. Dark lines show the negative vortex and gray lines the positive vortex.

Conclusions

A stereoscopic particle image velocimetry instrument has been constructed for a transonic wind tunnel to study the interaction created by a supersonic axisymmetric jet exhausting transversely from a flat plate into a transonic crossflow. Data have been acquired in the crossplane of the interaction at a single station in the far field, in which the streamwise direction is aligned with the out-of-plane velocity component. The resulting vector fields distinctly show the strength and location of the induced counter-rotating vortex pair as well as a second vortex pair within the wall boundary layer, which is the remnant of the horseshoe vortex that wraps around the jet plume as it first exhausts from the nozzle. Data taken for four different values of the jet-to-freestream dynamic pressure ratio J reveal the resulting change in the vortex characteristics as the relative strength of the jet is increased. At a single value of J, a sufficient quantity of data was gathered to compute all six unique components of the turbulent stress tensor, from which the mean spatial character of the turbulence was determined; these measurements may aid in selection of an appropriate turbulence model for simulations of this distinctly anisotropic flowfield.

Vorticity fields were derived from the in-plane velocity data, from which the strength, size, and position were determined for each of the two vortices in the counter-rotating vortex pair. These data reveal a small but significant asymmetry in the flowfield where the vortices are horizontally displaced off the nominal centerline of the interaction and one vortex appears slightly larger than the other; vortex strength differences are not significant within the measurement uncertainty. Further analysis shows that self-similarity is achieved in the lateral direction when dimensions are normalized either by the vortex diameter or the horizontal vortex spacing, and that comparable similarity is found in the wall-normal direction scaled with the vortex diameter once the vortex penetration is taken into account. Whereas past studies have shown that similarity in the

jet and vortex trajectories may be obtained when normalizing axes by J, the present work indicates that measures of the vortex size appear to be similar when normalized by $\sqrt{J}$. These analyses suggest means by which interaction properties may be related between different experimental configurations.

Acknowledgments

This work is supported by Sandia National Laboratories and the United States Department of Energy. Sandia is a multiprogram laboratory operated by Sandia Corporation, a Lockheed Martin Company, for the United States Department of Energy's National Nuclear Security Administration under Contract No. DE-AC04-94AL85000. The authors would like to thank W. L. Oberkampf, C. W. Peterson, and W. P. Wolfe, all of Sandia National Laboratories, for their helpful suggestions regarding this work.

References

[1] Cassel, L. A., Durando, N. A., Bullard, C. W., and Kelso, J. M., "Jet Interaction Control Effectiveness for Subsonic and Supersonic Flight," U. S. Army Missile Command, Report No. RD-TR-69-21, Redstone Arsenal, Sept. 1969.

[2] Dormieux, M., and Marsaa-Poey, R., "Numerical Assessment of Aerodynamic Interactions on Missiles with Transverse Jets Control," *Computational and Experimental Assessment of Jets in Cross Flow*, AGARD CP 534, 1993, pp. 30.1–30.11.

[3] Cassel, L. A., "Applying Jet Interaction Technology," *Journal of Spacecraft and Rockets*, Vol. 40, No. 4, 2003, pp. 523–537.

[4] Srivastava, B., "Aerodynamic Performance of Supersonic Missile Body- and Wing Tip-Mounted Lateral Jets," *Journal of Spacecraft and Rockets*, Vol. 35, No. 3, 1998, pp. 278–286.

[5] Brandeis, J., and Gill, J., "Experimental Investigation of Super- and Hypersonic Jet Interaction on Missile Configurations," *Journal of Spacecraft and Rockets*, Vol. 35, No. 3, 1998, pp. 296–302.

[6] Graham, M. J., Weinacht, P., and Brandeis, J., "Numerical Investigation of Supersonic Jet Interaction for Finned Bodies," *Journal of Spacecraft and Rockets*, Vol. 39, No. 3, 2002, pp. 376–383.

[7] Kamotani, Y., and Greber, I., "Experiments on a Turbulent Jet in a Cross Flow," *AIAA Journal*, Vol. 10, No. 11, 1972, pp. 1425–1429.

[8] Fearn, R., and Weston, R. P., "Vorticity Associated with a Jet in a Cross Flow," *AIAA Journal*, Vol. 12, No. 12, 1974, pp. 1666–1671.

[9] Margason, R. J., "Fifty Years of Jet in Cross Flow Research," *Computational and Experimental Assessment of Jets in Cross Flow*, AGARD CP 534, 1993, pp. 1.1–1.41.

[10] Fric, T. F., and Roshko, A., "Vortical Structure in the Wake of a Transverse Jet," *Journal of Fluid Mechanics*, Vol. 279, 1994, pp. 1–47.

[11] Kelso, R. M., Lim, T. T., and Perry, A. E., "An Experimental Study of Round Jets in Crossflow," *Journal of Fluid Mechanics*, Vol. 306, 1996, pp. 111–144.

[12] McCann, G. J., and Bowersox, R. D. W., "Experimental Investigation of Supersonic Gaseous Injection into a Supersonic Freestream," *AIAA Journal*, Vol. 34, No. 2, 1996, pp. 317–323.

[13] Santiago, J. G., and Dutton, J. C., "Velocity Measurements of a Jet Injected into a Supersonic Crossflow," *Journal of Propulsion and Power*, Vol. 13, No. 2, 1997, pp. 264–273.

[14] Beresh, S. J., Henfling, J. F., Erven, R. J., and Spillers, R. W., "Penetration of a Transverse Supersonic Jet into a Subsonic Compressible Crossflow," *AIAA Journal*, Vol. 43, No. 2, 2005, pp. 379–389.

[15] Beresh, S. J., Henfling, J. F., Erven, R. J., and Spillers, R. W., "Turbulent Characteristics of a Transverse Supersonic Jet in a Subsonic Compressible Crossflow," *AIAA Journal*, Vol. 43, No. 11, 2005, pp. 2385–2394.

[16] Haven, B. A., and Kurosaka, M., "Kidney and Anti-Kidney Vortices in Crossflow Jets," *Journal of Fluid Mechanics*, Vol. 352, 1997, pp. 27–64.

[17] Meyer, K. E., Ozcan, O., and Westergaard, C. H., "Flow Mapping of a Jet in Crossflow with Stereoscopic PIV," *Journal of Visualization*, Vol. 5, No. 3, 2002, pp. 225–231.

[18] Gogineni, S., Goss, L., Glawe, D., Bowersox, R., and Wier, R., "Digital Two-Color PIV and Flow-Visualization Studies for Complex Supersonic Flows," ASME Paper FEDSM97-3092, 1997.

[19] Mahmud, Z., and Bowersox, R., "Supersonic Missile Body Jet Interaction Flowfields at Low Momentum-Parameter-Ratio," AIAA Paper 2003-1244, Jan. 2003.

[20] Beresh, S. J., Henfling, J. F., Erven, R. J., and Spillers, R. W., "Stereoscopic PIV for Crossplane Vorticity Measurement of a Supersonic Jet in Subsonic Compressible Crossflow," AIAA Paper 2004-2181, June 2004.

[21] Samimy, M., and Lele, S. K., "Motion of Particles with Inertia in a Compressible Free Shear Layer," *Physics of Fluids A*, Vol. 3, No. 8, 1991, pp. 1915–1923.

[22] Melling, A., "Tracer Particles and Seeding for Particle Image Velocimetry," *Measurement Science and Technology*, Vol. 8, No. 12, 1997, pp. 1406–1416.

[23] Soloff, S. M., Adrian, R. J., and Liu, Z-C., "Distortion Compensation for Generalized Stereoscopic Particle Image Velocimetry," *Measurement Science and Technology*, Vol. 8, No. 12, 1997, pp. 1441–1454.

[24] Spaid, F. W., Zukoski, E. E., and Rosen, R., "A Study of Secondary Injection of Gases into a Supersonic Flow," NASA Technical Report No. JPL-32-834, Aug. 1966.

[25] Chocinski, D., "Contribution to the Modeling of Interactions of a Supersonic Jet in a Subsonic Compressible Crossflow," Doctoral Thesis, University of Poitiers, France, 1998.

[26] Chenault, C. F., Beran, P. S., and Bowersox, R. D. W., "Numerical Investigation of Supersonic Injection Using a Reynolds-Stress Turbulence Model," *AIAA Journal*, Vol. 37, No. 10, 1999, pp. 1257–1269.

[27] Beresh, S. J., Henfling, J. F., Erven, R. J., and Spillers, R. W., "Comparison of Data from Three PIV Configurations for a Supersonic Jet in Transonic Crossflow," *Proceedings of the 21st International Congress on Instrumentation in Aerospace Simulation Facilities*, Institute of Electrical and Electronics Engineers, New York, 2005, pp. 312–322.

[28] Smith, S. H., and Mungal, M. G., "Mixing, Structure, and Scaling of the Jet in Crossflow," *Journal of Fluid Mechanics*, Vol. 357, 1998, pp. 83–122.

[29] VanLerberghe, W. M., Santiago, J. G., Dutton, J. C., and Lucht, R. P., "Mixing of a Sonic Transverse Jet Injected into a Supersonic Flow," *AIAA Journal*, Vol. 38, No. 3, 2000, pp. 470–479.

[30] Keffer, J. F., and Baines, W. D., "The Round Turbulent Jet in a Cross-Wind," *Journal of Fluid Mechanics*, Vol. 15, 1963, pp. 481–496.

[31] Durando, N. A., "Vortices Induced in a Jet by a Subsonic Cross Flow," *AIAA Journal*, Vol. 9, No. 2, 1971, pp. 325–327.

[32] Broadwell, J. E., and Breidenthal, R. E., "Structure and Mixing of a Transverse Jet in Incompressible Flow," *Journal of Fluid Mechanics*, Vol. 148, 1984, pp. 405–412.

[33] Gruber, M. R., Nejad, A. S., Chen, T. H., and Dutton, J. C., "Mixing and Penetration Studies of Sonic Jets in a Mach 2 Freestream," *Journal of Propulsion and Power*, Vol. 11, No. 2, 1995, pp. 315–323.

[34] Pratte, B. D., and Baines, W. D., "Profiles of the Round Turbulent Jet in a Cross Flow," *Proceedings of the American Society of Civil Engineers: Journal of the Hydraulics Division*, Vol. 92, 1967, pp. 53–64.

N. Chokani
Associate Editor